Journal of Materials Chemistry A

Quantum-Cutting Yb3+-Doped Perovskite Nanocrystals for Monolithic Bilayer Luminescent Solar Concentrators

Journal:	*Journal of Materials Chemistry A*
Manuscript ID	TA-ART-02-2019-001261.R1
Article Type:	Paper
Date Submitted by the Author:	15-Mar-2019
Complete List of Authors:	Cohen, Theodore; University of Washington, Molecular Engineering and Science Institute; University of Washington, Chemistry; University of Washington, Materials Science and Engineering Milstein, Tyler; U. Washington, Seattle, Chemistry Kroupa, Daniel; U. Washington, Seattle, Chemistry MacKenzie, John; University of Washington, Materials Science & Engineering Luscombe, Christine; University of Washington, Materials Science & Engineering Gamelin, Daniel; U. Washington, Seattle, Chemistry

Quantum-Cutting Yb^{3+}-Doped Perovskite Nanocrystals for Monolithic Bilayer Luminescent Solar Concentrators

Theodore A. Cohen,[a,b,c] Tyler J. Milstein,[a] Daniel M. Kroupa,[a] J. Devin MacKenzie,[b,c] Christine K. Luscombe,[b,c] Daniel R. Gamelin[a,c,*]

[a.] *Department of Chemistry, University of Washington, Seattle, WA 98195-1700*

[b.] *Department of Materials Science and Engineering, University of Washington, Seattle WA 98195*

[c.] *Molecular Engineering and Sciences Institute, University of Washington, Seattle WA 98195*

[*] Email gamelin@uw.edu

Abstract. Luminescent solar concentrators (LSCs) can concentrate direct and diffuse solar radiation spatially and energetically to help reduce the overall area of solar cells needed to meet current energy demands. LSCs require luminophores that absorb large fractions of the solar spectrum, emit photons into a light-capture medium with high photoluminescence quantum yields (PLQYs), and do not absorb their own photoluminescence. Luminescent nanocrystals (NCs) with near or above unity PLQYs and Stokes shifts large enough to avoid self-absorption losses are well-suited to meet these needs. In this work, we describe LSCs based on quantum-cutting Yb^{3+}:$CsPb(Cl_{1-x}Br_x)_3$ NCs that have documented PLQYs as high as ~200%. Through a combination of solution-phase 1D LSC measurements and modeling, we demonstrate that Yb^{3+}:$CsPbCl_3$ NC LSCs show negligible intrinsic reabsorption losses, and we use these data to model the performance of large-scale 2D LSCs based on these NCs. We further propose a new and unique *monolithic bilayer* LSC device architecture that contains a Yb^{3+}:$CsPb(Cl_{1-x}Br_x)_3$ NC top layer above a second narrower-gap LSC bottom layer (*e.g.*, based on $CuInS_2$ NCs), both within the same waveguide and interfaced with the same Si PV for conversion. We extend the modeling to predict the flux gains of such bilayer devices. Because of the exceptionally high PLQYs of Yb^{3+}:$CsPb(Cl_{1-x}Br_x)_3$ NCs, the optimized bilayer device has a projected flux gain of 63 for dimensions of 70 x 70 x 0.1 cm^3, representing performance enhancement of at least 19% over the optimized $CuInS_2$ LSC alone.

Broader context (200 word limit). Nanocrystal (NC) luminescent solar concentrators (LSCs) represent a promising clean-energy technology capable of concentrating direct and diffuse light to reduce the area of photovoltaic (PV) cells – which are energetically costly to manufacture – required to meet energy demands. Recently, Yb^{3+}-doped $CsPb(Cl_{1-x}Br_x)_3$ perovskite NCs have been developed that convert single high-energy photons into pairs of low-energy photons, generating photoluminescence quantum yields approaching 200%. Here, we describe how this process – known as quantum cutting – can improve LSC efficiencies by simultaneously eliminating reabsorption and thermalization losses, and discuss the role of protons in the waveguide matrix. We further propose a fundamentally new monolithic bilayer LSC device architecture that capitalizes on the unique spectral properties of quantum-cutting Yb^{3+}-doped $CsPb(Cl_{1-x}Br_x)_3$ NCs by pairing them with a narrower-gap bottom LSC layer to enhance solar absorption within a single waveguide. This architecture overcomes a major limitation of conventional two-terminal tandem LSCs by eliminating the need for current matching, and can lead to marked performance improvements.

Introduction

Luminescent solar concentrators (LSCs) are passive concentrating devices that use luminophores embedded in transparent waveguides to redirect solar radiation from large areas onto the smaller areas of optically coupled photovoltaic (PV) cells.[1, 2] LSCs have been intensively researched for decades[3-7] because they can concentrate diffuse light with potentially unlimited flux gains[8-11] (ratio of photons converted by a given LSC-coupled PV to photons that would be converted by the same PV exposed directly to the same solar flux) using a collection waveguide fabricated from relatively low cost and low energy-to-manufacture per unit area materials. Recent models suggest that 100,000 square kilometers of conventional dense-cell solar-panel area would be required to meet current energy demands.[12] With an energy pay-back period for silicon PV that will likely remain on the order of several years,[13] LSCs are well suited

to reduce the total area of silicon PV cells required to meet energy demands.[2]

Most early work with LSCs used organic dyes as luminophores, and these LSCs have now been implemented in a variety of large-scale installations.[14-17] Recently, several inorganic semiconductor nanocrystals (NCs) with high photoluminescence quantum yields (PLQYs) have been explored for LSC applications, including various simple luminescent NCs,[18-23] as well as more complicated NC structures such as core/shell NCs,[24-28] dot-in-rod NCs,[29] and a variety of impurity- or defect-activated NCs.[30-40] Such semiconductor NCs can be made with less reabsorption of their own emission, larger absorption cross-sections, greater photochemical stability, and broader solar absorption than organic dyes. A survey[31] of several leading NCs showed that Mn^{2+}-doped[30, 31, 36] and Cu^{+}-doped[37, 41] NCs have substantially less intrinsic reabsorption than heterostructured NCs. $CuInE_2$ (E = S, Se) NCs have similar PL characteristics as Cu^{+}-doped NCs[42-45] and can be made with higher PLQYs. Consequently, LSCs based on $CuInE_2$ NCs have been heavily investigated[32-35, 38-40] and are currently being commercialized by UbiQD. Beyond Mn^{2+} and Cu^{+}, Yb^{3+} has been targeted as a NC dopant of particular interest for LSCs because its $^2F_{5/2} \rightarrow {}^2F_{7/2}$ *f-f* transition combines a narrow PL lineshape with high PLQYs and low *f-f* oscillator strengths (low reabsorption) at energies only slightly above the silicon band gap.[30] Several LSC designs employing Yb^{3+} luminescence have already been reported,[46-50] but the luminophores used to date have lower absorption cross sections than organic dyes or inorganic NCs. Attempts at sensitizing Yb^{3+} luminescence using intermediate-gap semiconductor NCs have been moderately successful,[51-53] but none of these materials were sufficiently promising until the recent development of Yb^{3+}:$CsPbX_3$ perovskite NCs, which show highly efficient picosecond quantum cutting that generates PLQYs approaching the quantum-cutting limit of 200%.[54-56]

Although quantum-cutting Yb^{3+}-doped $CsPbX_3$ NCs have reabsorption-minimizing effective Stokes shifts and unprecedented PLQYs for doped NCs, the energy-conservation requirement of quantum cutting limits their solar absorption to $\lambda < \sim 500$ nm.[55, 56] This limitation mirrors the challenges faced by high-band-gap PV materials, which have therefore emerged as candidates for alternative configurations including tandem or multi-junction PV cells.[57-61] The tandem concept has already been explored in LSCs based on organic[62-64] or inorganic[18, 27, 40, 65, 66] luminophores. Here, a top LSC coupled to a wider-gap PV is placed above a separate bottom LSC coupled to a lower-gap PV and the PV voltages are summed, allowing bluer photons to be converted with greater energy efficiency than in a single-layer LSC. Two-terminal tandem devices require near-perfect photocurrent matching between the top and bottom cells under all operating conditions to prevent the closed-circuit current from being limited by the lowest performing PV cell, however. Photocurrent losses are observed even in state-of-the-art two-terminal tandem PV cells,[59-61] and this challenge has not been addressed in the tandem LSC literature.

In this work, we use a 120 cm 1D LSC[31, 32] to demonstrate that Yb^{3+}:$CsPbCl_3$ NCs indeed behave as zero-reabsorption, high-efficiency luminophores suitable for application in large-scale LSCs. We show that Yb^{3+}:$CsPbCl_3$ NCs have negligible intrinsic attenuation losses over these large waveguide lengths, but also that severe attenuation is still observed when the waveguide contains C-H bonds (high-frequency vibrations). This result has important implications for future large-scale LSC work involving these materials, because it precludes the use of popular acrylics as waveguides. With these results in hand, we further propose and model a new monolithic-bilayer LSC device architecture integrating quantum cutting that offers an attractive alternative to traditional tandem LSCs. This new device concept is fundamentally different from tandem

LSCs in that the concentrated photons from both luminophore layers are all directed *via* the same waveguide to the same PV, circumventing the expenses and technical challenges associated with current matching in normal tandem devices. For illustration, we model integration of a layer of band-gap-optimized Yb^{3+}:$CsPb(Cl_{1-x}Br_x)_3$ NCs on top of a state-of-the-art $CuInS_2$ NC LSC in a monolithic bilayer configuration and predict improvement of overall LSC performance by at least 19%. These results identify both practical guidelines and conceptual directions for future LSC development that can capitalize on the unique spectroscopic and photophysical properties of quantum-cutting Yb^{3+}:$CsPb(Cl_{1-x}Br_x)_3$ NCs.

Experimental

Materials. Lead acetate trihydrate [$Pb(OAc)_2 \cdot 3H_2O$] (99.9%, Baker Chemical), ytterbium acetate hydrate [$Yb(OAc)_3 \cdot xH_2O$] (99.9%, Strem Chemical), cesium acetate [CsOAc] (99.9%, Alfa Aesar), anhydrous ethanol (200 proof, Decon Laboratories, Inc.), chlorotrimethylsilane (TMS-Cl) (98%, Acros Organics), bromotrimethylsilane (TMS-Br) (97%, Sigma Aldrich), 1-octadecene (ODE) (90%, Sigma Aldrich), oleylamine (OAm) (70%, Sigma Aldrich), oleic acid (OA) (90%, Sigma Aldrich), hexanes (99%, Sigma Aldrich), tetrachloroethylene (TCE) (99%, Alfa Aesar), anhydrous ethyl acetate (99%, Sigma Aldrich), and 1/4" and 1/8" extruded poly(methyl methacylate) (PMMA) slabs (Evonik Cyro LLC) were used as received unless otherwise noted.

Nanocrystal synthesis and purification. Yb^{3+}:$CsPbCl_3$ NCs with the highest Yb^{3+} emission quantum yield were synthesized by hot-injection following procedures reported elsewhere.[55] Samples suspended in TCE were not filtered after washing and purification. To synthesize the mixed Yb^{3+}:$CsPb(Cl_{1-x}Br_x)_3$ NCs, a freshly synthesized Yb^{3+}:$CsPbCl_3$ NC sample in hexane was transferred into an N_2 filled glovebox. Small amounts of 1 M TMS-Br in hexane were titrated into the NC sample until the absorption onset reached 488 nm.[67]

Physical measurements. Optical absorption spectra in the visible regime that require a 1 cm cuvette were collected at room temperature using a Cary 60 spectrometer. All other optical absorption spectra were collected at room temperature using a Cary 5000 spectrometer.

Wavelength independent absorption constants were added to the absorption spectra of hexanes and TCE to account for reflection losses. NC transmission electron microscopy (TEM) images were collected using a FEI TECNAI F20 microscope at 200 kV. TEM samples were prepared by drop casting NC suspensions onto carbon-coated copper grids from TED Pella, Inc. Powder X-ray diffraction (XRD) spectra were collected using a Bruker D8 Advance diffractometer. Samples were prepared by drop-casting NC suspensions onto monocrystalline silicon wafer substrates. Samples were irradiated using Cu Kα radiation (50 W). Photoluminescence spectra for photoluminescence quantum yield (PLQY) and 1D LSC experiments were collected using a monochromator coupled to a spectrally corrected nitrogen-cooled CCD. PLQY measurements were performed according to the procedures described previously.[55] Elemental compositions were determined by inductively coupled plasma – atomic emission spectroscopy (ICP-AES, PerkinElmer 8300). Samples were prepared by digesting the NCs in concentrated nitric acid overnight with sonication. Yb^{3+} atomic concentrations are defined as $[Yb^{3+}]/([Yb^{3+}] + [Pb^{2+}])$.

1D LSC measurements. The apparatus for measuring LSC reabsorption losses used here is based on a 120 cm long hollow quartz waveguide (Friederick and Dimmock Co.) with a 1 mm x 1 mm square inner dimension and 1.65 mm x 1.65 mm outer dimension, suspended over a black aluminum channel. The quartz tube was filled with sample using a removable capillary tube. A 375 nm pulsed laser passed through an iris at its smallest setting was used as the excitation source. Emission from the 1D LSC is treated as a point source and was collected using our homebuilt CCD setup. The excitation source distance from the closed end of the tube was varied by moving the laser across the laser table and aligning the laser perpendicular to the tube to maximize signal.

Results and Analysis

I. Nanocrystal characterization and 1D LSCs

Figure 1a shows representative absorption and PL spectra of Yb^{3+}:$CsPbCl_3$ NCs dispersed in hexane, and compares these spectra with the external quantum efficiency (EQE) of a near infrared (NIR) enhanced Si HIT PV cell[61] and the AM 1.5 solar spectrum.[68] The analytical atomic Yb^{3+} B-site concentration for these NCs was 5.4%, and the PLQY was measured to be

130% at a CW excitation rate ~ 350 s^{-1}. The NCs absorb UV light in a region where the Si PV EQE is poor, and they reemit this energy in a region where the Si PV EQE ~ 1. Figure 1b shows a representative TEM image of a sample of Yb^{3+}:$CsPbCl_3$ NCs. The NCs display the characteristic cube-like shapes of the parent $CsPbCl_3$ NCs. Figure 1c shows representative XRD data demonstrating that the perovskite crystal structure was indeed synthesized. The reproducibility of this synthesis was validated in our previous report.[55]

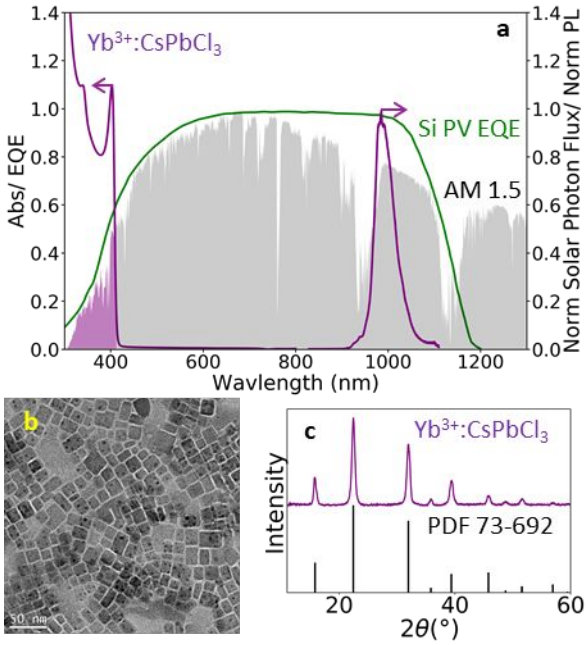

Figure 1. (a) Absorption and normalized PL spectra of Yb^{3+}:$CsPbCl_3$ NCs (purple) plotted with the EQE of a NIR enhanced Si HIT PV (green) and the AM1.5 solar spectrum (shaded area). Spectra were collected at room temperature. **(b)** TEM and **(c)** XRD data for a representative sample of Yb^{3+}:$CsPbCl_3$ NCs.

Undoped perovskite NCs,[66, 69, 70] thin films,[71] and Mn^{2+}-doped $CsPbCl_3$ NCs[36] have been used in LSCs previously. While this manuscript was under preparation, a small-scale (5 cm x 5 cm) LSC using these same quantum-cutting Yb^{3+}:$CsPbCl_3$ NCs was also reported.[72] This report supports the premise that Yb^{3+}:$CsPbCl_3$ NCs are attractive for LSCs, as anticipated from their spectroscopy, but it does not assess any of the fundamental loss mechanisms that *are* active

within such LSCs, and it does not evaluate performance in waveguides beyond the 5 cm x 5 cm model LSC. Because the key attraction of LSCs is their ability to harvest photons over large LSC facial areas for concentration into small PV areas, it is important to evaluate the photon losses in larger waveguides, for example on the scale of a building's windows.[3, 4, 39] To this end, measurements were performed here on Yb^{3+}:$CsPbCl_3$ NCs in a substantially larger waveguide than investigated previously.

Figure 2a plots normalized experimental PL spectra collected in a (120 cm) × $(1\ mm)^2$ 1D LSC at various excitation distances away from the LSC edge, where the photodetector is mounted (complete PL intensity data are provided in the Supplementary Information, Figure S1). For these measurements, Yb^{3+}:$CsPbCl_3$ NCs were suspended in hexane with a transverse optical density (OD_t) of ~0.75 mm^{-1} at 375 nm (see Supplementary Information for complete visible absorption spectra, Figure S2). Figure 2b plots the integrated intensities of the raw PL traces as a function of excitation distance, normalized to the integrated PL intensity at the shortest excitation distance. These data show substantial attenuation of the PL as the distance traveled by emitted photons to the detector through the waveguide is increased. For comparison, Figure 2b also plots the experimentally determined waveguide attenuation over these extremely large waveguide lengths,[31] reflecting photon scattering and otherwise imperfect transmission even in the absence of NCs. The curve plotted here was obtained by fitting the 1D LSC attenuation data (see Supplementary Information, Figure S3), which yielded a wavelength-independent attenuation coefficient of 0.002 cm^{-1}. This curve represents the performance limit of this particular 1D LSC waveguide, and it allows the intrinsic NC performance to be assessed. These results show that the experimental Yb^{3+} PL attenuation is not due to waveguide losses. As independent confirmation, Figure 2b also plots analogous 1D LSC data collected for the same NCs diluted by

a factor of 10. These LSC data are essentially indistinguishable from the higher-concentration data, indicating substantial attenuation that is *not* caused by the NCs themselves. Instead, this attenuation can be traced to absorption of the Yb^{3+} PL by vibrational bands of the organic medium containing the NCs in this 1D LSC. Figure 2a also plots the absorption spectrum of hexane in the wavelength region of the Yb^{3+} PL and reveals a series of weak but significant vibrational overtone bands characteristic of C-H stretching vibrations.[73] The data in Figure 2a show that the Yb^{3+} PL intensity is attenuated on its red and blue edges with increasing waveguide length, precisely where this PL overlaps with these vibrational overtone bands.

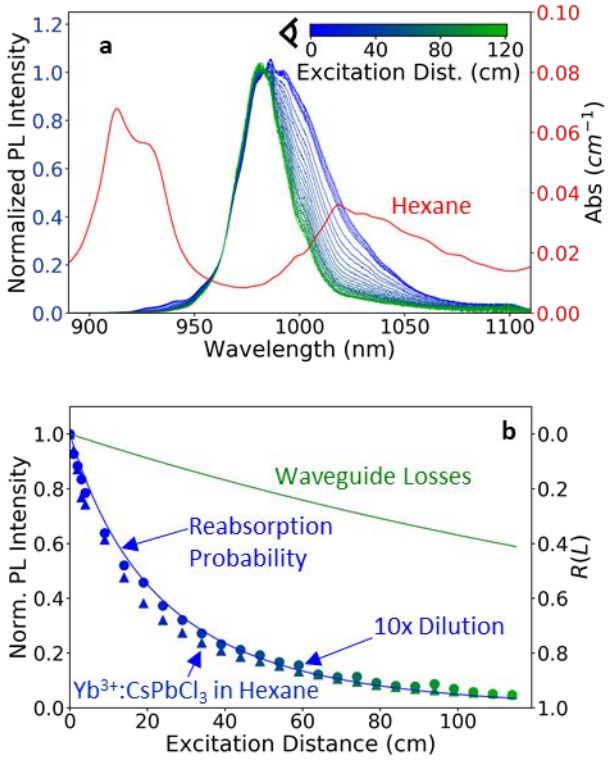

Figure 2. (a) Normalized PL spectra of Yb^{3+}:$CsPbCl_3$ NCs suspended in hexane with $OD_t \sim 0.75$ mm^{-1} at 375 nm, obtained from the 1D LSC experiment at various excitation distances relative to the edge-mounted photodetector (see inset). The red curve shows the absorption spectrum of the hexane solvent. **(b)** Integrated normalized Yb^{3+}:$CsPbCl_3$ NC PL intensity plotted as a function of excitation distance away from the photodetector, for NCs in hexane with $OD_t \sim 0.75$ mm^{-1} (triangles) and $OD_t \sim 0.075$ mm^{-1} (circles) at 375 nm. The blue trace is the reabsorption probability described in eq 1 modeled with hexane absorption from Figure 2a. The green line is the experimentally determined performance limit of the 1D LSC. All PL data were collected with excitation at 375 nm, and all data

were collected at room temperature.

For quantitative data analysis, these 1D LSC data were modeled following methods adapted from our previous work.[31, 32] Briefly, the PL reabsorption probability is described by eq 1,

$$R(L) = \int PL_{norm}(\lambda)\left(1 - 10^{\frac{-A_{norm}(\lambda) L\, OD_t}{t}}\right)d\lambda \quad (1)$$

where $A_{norm}(\lambda)$ is the absorption spectrum of the NCs, solvent, and waveguide normalized at 375 nm, t is the thickness of the NC layer in the 1D LSC (t = 1.0 mm here), OD_t is the optical density over that thickness at the excitation wavelength of 375 nm, L is the excitation distance away from the LSC collection edge, and $PL_{norm}(\lambda)$ is the amplitude of the area-normalized NC PL spectrum measured at λ. Using eq 1, the hexane absorption spectrum, and the PL spectrum at L = 0 from Figure 2b, the attenuation of the integrated Yb^{3+} luminescence intensity as a function of L was simulated. The resulting curve is included in Figure 2b along with the experimental data, and good agreement between the two is observed. Overall, this analysis confirms that the PL attenuation in this experiment is not due to losses involving the NCs or the glass portion of the waveguide, but instead comes from absorption of emitted photons by C-H vibrations of the organic portion of the waveguide, and it allows quantitative description of these contributions to the overall LSC performance.

To eliminate the C-H absorption losses identified above, Yb^{3+}:$CsPbCl_3$ NCs were suspended in tetrachloroethylene (TCE), which lacks protons and is therefore transparent in the NIR window of interest. Figure 3a plots the Yb^{3+} PL intensity measured as a function of excitation distance for 1D LSC measurements with this solvent. For comparison, the corrected absorption spectrum of TCE is also included in Figure 3a. Because TCE has no C-H vibrational

overtone bands in the NIR, the Yb^{3+} PL intensity decay is now independent of wavelength. For comparison, Figure 3b plots the integrated PL intensities *vs* excitation distance for the same NC concentration in both TCE and hexane (see Supplemental Information for absorption spectra, Figure S2). The PL intensity from the TCE solution is substantially greater at large excitation distances than that from the hexane solution under similar conditions. In fact, the integrated PL intensity from the TCE solution essentially follows the waveguide losses of the 1D LSC alone, indicating that this decay now comes primarily from scattering within the glass waveguide. These NCs show reabsorption losses as low as any of the NCs measured previously over similar 120 cm waveguide lengths.[31, 32]

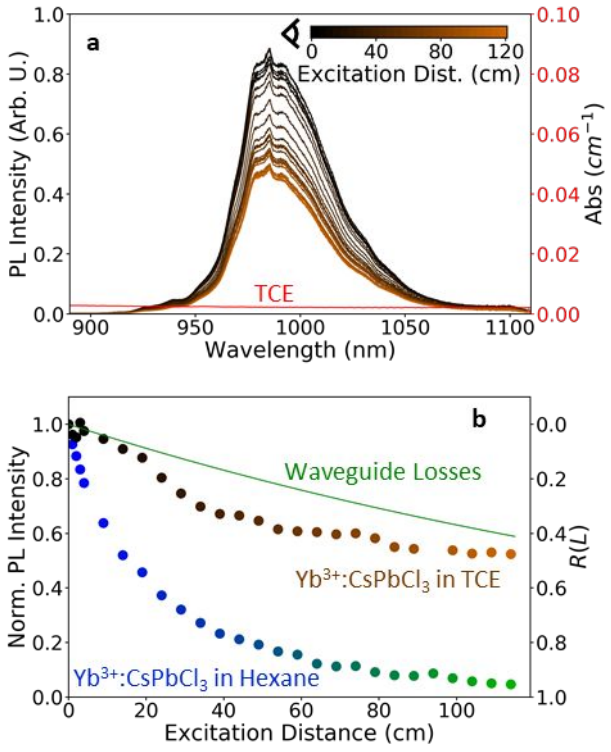

Figure 3. (a) PL intensity of Yb^{3+}:$CsPbCl_3$ NCs suspended in tetrachloroethylene (TCE) from the 1D LSC experiment plotted from low excitation distances to high excitation distance with the corrected absorption spectrum of TCE. **(b)** Integrated normalized PL intensity of Yb^{3+}:$CsPbCl_3$ NCs plotted as a function of excitation distance for solutions in hexane with an $OD_t \sim 0.075$ mm^{-1} (blue-green) and in TCE with an $OD_t \sim 0.075$ mm^{-1} (black-brown). The green line is the experimentally determined performance limit of the 1D LSC. The analytical atomic Yb^{3+} concentration for these NCs was 4.6% and the

PLQY was 138% in hexane and 71% after transfer to TCE.

Figure 4a shows the absorption spectra of hexane and two potential waveguide materials (PMMA and Schott optical-quality glass) overlaid with the Yb^{3+} PL spectrum from these Yb^{3+}:$CsPbCl_3$ NCs. The PMMA spectrum is similar in magnitude and shape to those reported previously,[73, 74] and in particular, it shows C-H vibrational overtone absorption bands similar to those observed in hexane, shifted slightly to shorter wavelength and still overlapping the Yb^{3+} PL substantially. In contrast, the Schott glass shows little to no absorption in this region.

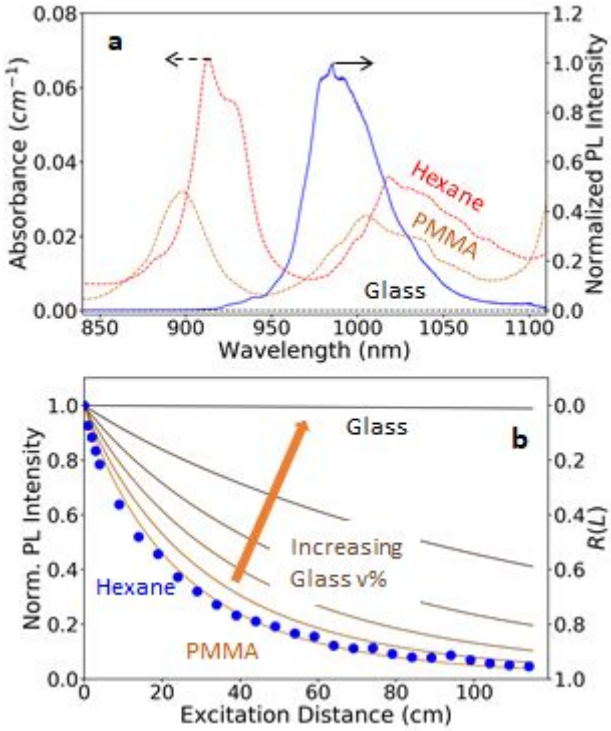

Figure 4. (a) Absorption spectrum of hexane (red), a representative PMMA sample (orange), and Schott optical-quality glass (black) overlaid with the normalized PL spectrum of Yb^{3+}:$CsPbCl_3$ NCs (blue). The PMMA spectrum was obtained by subtracting experimental spectra measured for two samples with different thickness to eliminate surface reflection and scattering effects. **(b)** Normalized PL intensity of Yb^{3+}:$CsPbCl_3$ NCs in hexane as a function of excitation distance in a 120 cm-long 1D LSC (blue dots). The curves plot absorption probabilities for the Yb^{3+}:$CsPbCl_3$ NC PL waveguided through glass (black) and PMMA (orange) calculated using eq 1. The intermediate traces show the absorption probabilities in hypothetical mixed PMMA/glass waveguides with volume percentages increasing from 0% to 100% by increments of 20%.

With these spectra, it is possible to simulate the anticipated performance of various acrylic and glass 1D LSCs, as well as of composite (or layered) waveguides involving different volume fractions of polymer and glass as per common 2D LSC configurations. An attenuation coefficient of 4.14 x 10^{-5} cm^{-1} was used to model transmission through glass in these simulations.[75] Figure 4b plots the results of these calculations. From these simulations, the NC performance in a PMMA waveguide will likely be as poor as the experimental 1D LSC results in hexane reported in Figure 3b (and reproduced in Figure 4b for comparison). These results relate to the recent report of a small-scale LSC made from suspension of Yb^{3+}:$CsPbCl_3$ NCs in PMMA. The data from this device were fitted to conclude a wavelength-independent attenuation coefficient of 0.023 cm^{-1},[72] which the authors attributed to scattering and suggested could be eliminated through device optimization. The results in Figure 4a show, however, that the PMMA absorbance itself is ~0.02 cm^{-1} where it overlaps the Yb^{3+} PL, and this absorption is not wavelength independent. This analysis thus indicates that popular acrylics will likely not be suitable waveguide matrices for LSCs based on Yb^{3+} emission, including from quantum-cutting Yb^{3+}:$CsPb(Cl_{1-x}Br_x)_3$ NCs. In contrast, the performance of Yb^{3+}:$CsPb(Cl_{1-x}Br_x)_3$ NC LSCs using glass waveguides will likely be near the theoretical limit. Figure 3b further illustrates that a device configuration involving a thin PMMA film containing densely packed NCs on top of a glass waveguide falls between these two extremes, with LSC performance determined by the relative PMMA and glass waveguide volumes. Clearly, this layered PMMA/glass LSC configuration is only attractive with Yb^{3+}:$CsPb(Cl_{1-x}Br_x)_3$ NCs if the PMMA film is very thin relative to the glass waveguide (*e.g.*, <~5% PMMA by volume).

II. 2D LSCs

Monolayer 2D LSCs. As detailed previously,[31, 32] 1D LSC data and simulations of the type presented above provide all of the necessary input to assess the 2D LSC performance of a given luminophore. The primary metric of interest is the LSC flux gain (*FG*), defined as the ratio of photons converted by a given LSC-coupled PV to photons that would be absorbed by the same PV exposed directly to the same solar flux. The 2D LSC flux gain (FG_{2D}) is calculated using eq 2,

$$FG_{2D} = OQE(L)\frac{\eta_{pl}\ A_{nc}}{\eta_{AM}A_{sol}}G(L) \quad (2)$$

where η_{nc} is the NC PLQY, η_{pl}/η_{AM} is the efficiency of a silicon PV exposed to the NC PL spectrum relative to the efficiency of the same PV exposed to AM 1.5 solar radiation. $G(L)$ is the LSC geometric gain, equal to $L/4t$, where L is the edge length and t is the waveguide thickness in a square 2D device. The optical quantum efficiency $OQE(L)$ is the ratio of photons that reach the LSC edge to solar photons absorbed by the LSC, A_{nc} is the solar flux absorbed by a particular NC LSC, and A_{sol} is the solar flux absorbed by the solar cells coupled to the edges of the device when directly exposed to the solar irradiation. A_{nc} and A_{sol} are calculated using eqs 3 and 4,

$$A_{nc} = \int \Phi_{AM1.5}(\lambda)\left(1 - 10^{-A_{abs}(\lambda)}\right)d\lambda \quad (3)$$

$$A_{sol} = \int \Phi_{AM1.5}(\lambda)EQE(\lambda)d\lambda \quad (4)$$

where $\Phi_{AM1.5}$ is the AM1.5 solar photon flux, $A_{abs}(\lambda)$ is the NC absorption spectrum, $EQE(\lambda)$ is the external quantum efficiency of the solar cell of interest. The 1D LSC results presented in Figure 3b suggest that there are no reabsorption losses for the Yb^{3+}:$CsPbCl_3$ layer. Therefore, $OQE(L)$ can be calculated using eq 5.

$$OQE(L) = \frac{\Phi}{4\pi L^2} \iint_{L \times L} \int_0^{2\pi} \int_{\varphi_{esc}}^{\pi - \varphi_{esc}} I_{PL}(l(x,y,\theta,\varphi)) sin\varphi d\varphi d\theta dx dy \quad (5)$$

Here, $l(x, y, \theta, \varphi)$ is the distance a photon must travel from any point $x,y \in [0, L]$, any azimuthal angle $\theta \in [0, 2\pi]$, and any polar angle $\varphi \in [\varphi_{esc}, \varphi_{esc} - \pi]$, Φ is the NC PLQY, $I_{PL}(L)$ is the normalized, integrated PL intensity as a function of excitation distance from a collection edge (obtained from the 1D LSC experimental data), and φ_{esc} is the polar angle that defines the photon escape cone, which equals $\arcsin\left({}^{1}/_{n}\right)$, where n is the waveguide's refractive index.

The flux gain of an Yb^{3+}:$CsPbCl_3$ NC 2D LSC was calculated using eqs 2-5 using the experimental data from Figure 3b as input (or extrapolated from these data for waveguiding lengths exceeding 120 cm). In this simulation, a value of Φ = 170% was used, based on experiment,[55] and *n* was assumed to be 1.5, which is the approximate refractive index of glass or PMMA.[6] Si HIT PV cells provide the best spectral matching with these Yb^{3+}:$CsPbCl_3$ NCs, and these PV have ${}^{\eta_{pl}}/_{\eta_{AM}} \sim 1$ because of their high NIR EQE. $OQE(L)$ for the Yb^{3+}:$CsPbCl_3$ NCs was calculated using eq 5. As validation, average distances to the edge of a square calculated using $l(x,y,\theta,\varphi)$, along with 2D flux-gain predictions for $Zn_{0.87}Cd_{0.11}Mn_{0.02}Se$/ZnS NCs that match our previous report,[31] are provided as Supplementary Information (Figure S4). Figure 5c (*vide infra*) summarizes the results of these simulations up to a geometric gain of 175. The initial slope of the flux gain trace for a Yb^{3+}:$CsPbCl_3$ NC 2D LSC is 0.06, and the maximum projected flux gain is 8 at G = 175. This value is substantially larger than the projected gain of 5 for a $Zn_{0.87}Cd_{0.11}Mn_{0.02}Se$/ZnS NC LSC simulated by the same methods,[30, 31] despite the fact that Yb^{3+}:$CsPbCl_3$ NCs absorb 30% fewer AM1.5 solar photons than $Zn_{0.87}Cd_{0.11}Mn_{0.02}Se$/ZnS NCs do. These results demonstrate that even with their wide energy gap, Yb^{3+}:$CsPbCl_3$ NCs can excel

as luminophores for 2D LSCs because of their exceptionally high PLQYs resulting from quantum cutting.

Bilayer 2D LSCs. (*i*) *Yb^{3+}:$CsPbCl_3$/$CuInS_2$ bilayers.* Although Yb^{3+}:$CsPbX_3$ NC LSCs themselves have inherent advantages over other LSCs arising from their unusual quantum-cutting capabilities, we propose that the greatest advantage can be taken of these materials if they are paired with another set of narrower-gap NCs in the same waveguide to form a new type of monolithic bilayer LSC. Figure 5a illustrates the proposed device structure. In this configuration, high-energy light is absorbed by the quantum-cutting Yb^{3+}:$CsPbCl_3$ NCs. Lower-energy light is transmitted by the top layer and absorbed in the bottom layer, which may use any of several available broadband LSC luminophores. $CuInS_2$ and related NCs have emerged as particularly attractive materials for LSCs because of their high PLQYs, broadband absorption across the visible, and large effective PL Stokes shifts;[32, 35, 38-40] for illustrative purposes, we consider these for the bottom layer of the proposed device. Figure 5b plots relevant absorption and PL spectra for this device architecture. $CuInS_2$/ZnS NC absorption and PL spectra are reproduced from a recent report of high-performance NC LSCs.[39] Importantly, although the Yb^{3+}:$CsPbCl_3$ and $CuInS_2$/ZnS NCs are layered such that bluer photons are absorbed by the top-layer Yb^{3+}:$CsPbCl_3$ NCs, and transmitted redder photons are absorbed by the bottom-layer $CuInS_2$/ZnS NCs, both layers emit in the NIR at wavelengths that can be transmitted through *both* absorber layers of this waveguide. Like two-terminal tandem LSCs investigated previously,[18, 27, 40, 62-66] this bilayer device structure improves LSC efficiency by eliminating thermalization losses associated with the blue photons. Unlike two-terminal tandem LSCs, however, this structure has the distinct advantage that it avoids the use of two separate LSCs that use separate PV cells wired in series. For maximum efficiency, the tandem configuration would require current matching between the

two LSC layers. In the monolithic bilayer configuration, it is the currents that are added at the fixed voltage of the single edge-mounted PV, vastly simplifying the device.

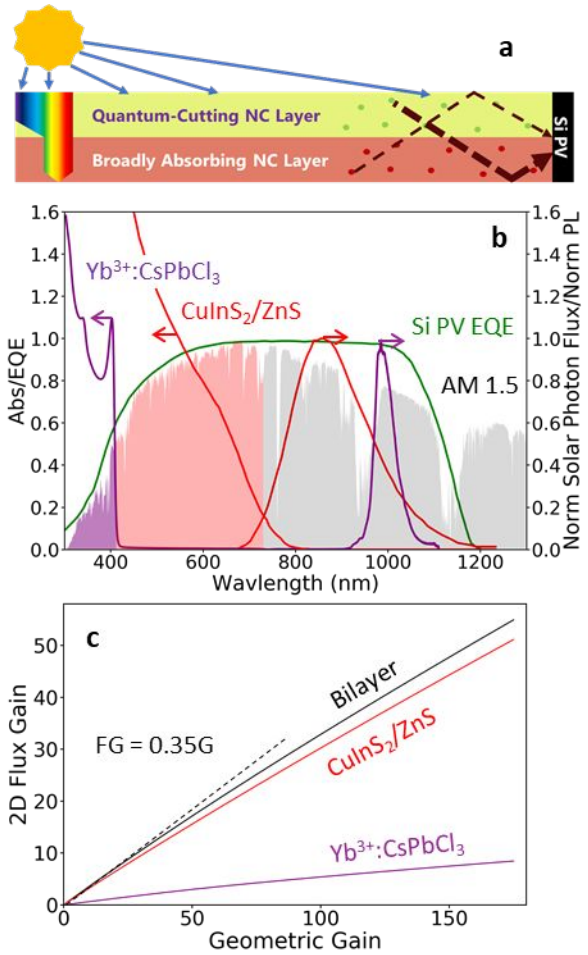

Figure 5. (a) Schematic of the proposed monolithic bilayer LSC. The top layer contains quantum-cutting NCs (*e.g.,* Yb^{3+}:$CsPb(Cl_{1-x}Br_x)_3$ NCs) and the bottom layer contains broadly absorbing NCs (*e.g.,* $CuInS_2$ NCs). **(b)** Absorption and normalized PL spectra of Yb^{3+}:$CsPbCl_3$ NCs (purple) and $CuInS_2$/ZnS NCs (red) overlaid with the AM 1.5 solar spectrum (shaded area) and the external quantum efficiency (EQE) of a NIR enhanced Si HIT PV (green). **(c)** Projected 2D flux gain of a Yb^{3+}:$CsPbCl_3$ NC LSC (purple), a $CuInS_2$/ZnS NC LSC (red), and the monolithic, bilayer device shown in Figure 5a (black).

To explore the potential benefits that might be expected from such a quantum-cutting bilayer LSC, the experimental data described above were used to model the performance of 2D Yb^{3+}:$CsPbCl_3$ NC/$CuInS_2$ NC bilayer LSCs in the configuration illustrated in Figure 5a. The flux

gains of Yb^{3+}:$CsPbCl_3$/$CuInS_2$ NC-based bilayer 2D LSCs were calculated using eqs 2-5. In these simulations, a value of Φ = 91% was used for the for $CuInS_2$ NCs, based on the highest reported literature value (obtained with $CuInS_2$/ZnS core/shell NCs).[39] η_{pl}/η_{AM} was again assumed to be ~1 due to the high NIR EQE of the Si HIT cells. For $CuInS_2$ NCs, an additional OD of 0.002 cm^{-1} was added to the attenuation spectrum to simulate the impact of waveguide losses on the projected flux gain (reabsorption probability simulations provided in Supplementary Information, Figure S5). Because reabsorption losses will affect the performance of the $CuInS_2$ layer, the $OQE(L)$ of the $CuInS_2$ layer is computed using an advanced analytical model developed previously.[38] A detailed description of this model is provided in the Supplementary Information.

To simulate the performance of the bilayer LSC of Figure 5a, the thickness of each waveguide layer was assumed to be 0.5 mm and the optical density of each layer was doubled compared to its single-layer analog. From here, the solar flux absorbed by the $CuInS_2$ NCs in the bilayer device is the difference between A_{CIS} and A_{CsPbCl_3}. Once this modification is made, the flux gain of the bilayer device is simply the sum of the Yb^{3+}:$CsPbCl_3$ NC LSC flux gain and the $CuInS_2$ NC LSC flux gain. Figure 5c summarizes the results of these simulations. The bilayer device reaches a flux gain of 55 for G = 175, which is a 7% improvement over the $CuInS_2$ NC LSC of similar dimensions. The initial slope of the bilayer device is 0.35, compared with 0.06 for the Yb^{3+}:$CsPbCl_3$ NC LSC or 0.32 for the $CuInS_2$ NC LSC alone.

(*ii*) *Yb^{3+}:$CsPb(Cl_{1-x}Br_x)_3$/$CuInS_2$ bilayers.* Improved solar absorption can be achieved by narrowing the top layer's energy gap through anion alloying. Figure 6a shows the absorption and PL spectra of Yb^{3+}:$CsPb(Cl_{1-x}Br_x)_3$ NCs synthesized from Yb^{3+}:$CsPbCl_3$ NCs *via* anion exchange.[67, 76] Increasing x to ~0.75 decreases the NC energy gap to ~488 nm (~2.5 eV) and

increases the fraction of the solar spectrum absorbed from ~2.6% (x = 0) to ~8.3% without impacting the PLQY of the Yb^{3+} emission.[67] Figure 6b plots the results of this model for three values of the perovskite absorption threshold, from 412 nm (x = 0) to 488 nm (x ~ 0.75), calculated by modifying $A_{CsPb(Cl_{1-x}Br_x)_3}$ in eq 3. Narrowing the perovskite energy gap increases the initial flux-gain slope of the stand-alone Yb^{3+}:$CsPb(Cl_{1-x}Br_x)_3$ NC LSC from 0.06 to 0.20 and increases the flux-gain to 27 at G = 175. The initial flux-gain slope of the bilayer device increases from 0.35 to 0.43 and the flux gain increases to 63 at G = 175. This result means that for the modeled 70 x 70 x 0.1 cm^3 monolithic bilayer LSC, the 28 cm^2 of Si solar cells optically coupled to its edges are predicted to generate 63 times more current than when the same solar cells are operating in non-concentrating conditions. These results represent a 19% performance increase compared with state-of-the-art $CuInS_2$ NC LSCs. The percentage improvement will be even greater if the PLQY of the $CuInS_2$ NC layer is not the record 91% but closer to the ~70% typically found for $CuInS_2$ NC/polymer composites.[38-40]

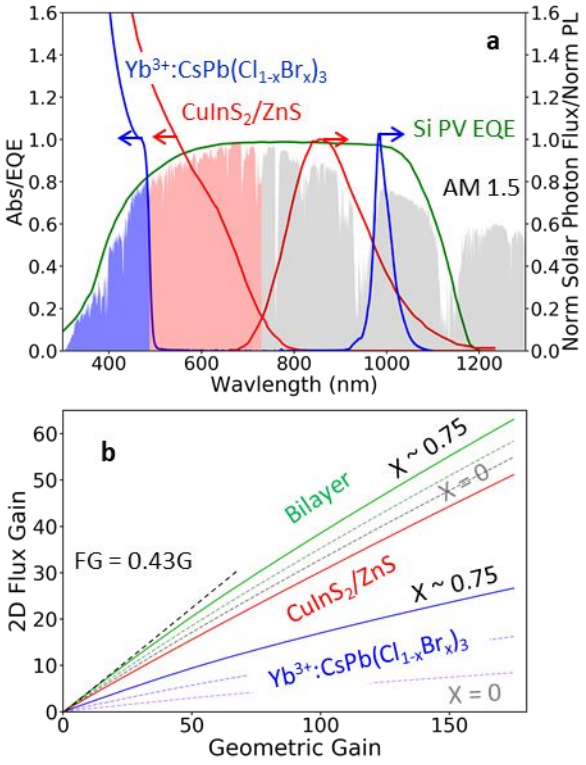

Figure 6. (a) Absorption and normalized PL spectra of Yb^{3+}:$CsPb(Cl_{1-x}Br_x)_3$ NCs with $x \sim 0.75$ (blue) and $CuInS_2$/ZnS NCs (red) overlaid with the AM 1.5 solar spectrum (shaded area) and the external quantum efficiency (EQE) of a NIR enhanced Si HIT PV (green). **(b)** Projected 2D flux gain of a Yb^{3+}:$CsPb(Cl_{1-x}Br_x)_3$ NC LSC (purple to blue gradient), a $CuInS_2$/ZnS NC LSC (red), and the monolithic, bilayer device shown in fig. 5a (black to green). The absorption onset of the Yb^{3+}:$CsPb(Cl_{1-x}Br_x)_3$ NCs is varied linearly from 412 nm to 488 nm for the three plotted traces.

We note that the $CuInS_2$ NCs used in ref. [39] and modeled above were likely optimized for a polycrystalline Si PV, whereas narrower-gap $CuIn(S_{1-y}Se_y)_2$ NCs may be more appropriate for the Si HIT PV simulated here. To assess the effect of increasing solar absorbance through this change, we modeled the performance of the same bilayer LSC but using the absorption and emission spectra of QD-950 from the Strem catalog[77] (absorption and PL spectra provided as Supporting Information, Figure S6a). Although the solar absorbance of the QD-950 NCs does increase from 26% to 38%, the flux gain of the Yb^{3+}:$CsPb(Cl_{1-x}Br_x)_3$ NC monolithic bilayer device *decreases*, *e.g.*, from 63 to 54 at $G = 175$ (see Supporting Information, Figure S6b), despite again assuming a PLQY of 91%. We attribute this lack of improvement to increased reabsorption losses in the QD-950 NCs because of their more pronounced absorption tail. Nonetheless, the flux gain of the monolithic bilayer LSC involving a QD-950 NC bottom layer is improved by 35% over the optimized QD-950 NC 2D LSC alone, again validating the bilayer LSC configuration as a simple and attractive opportunity for next-generation NC LSCs.

Discussion

The experimental results described above demonstrate superb performance of Yb^{3+}-doped halo-perovskite NCs as zero-reabsorption luminophores for large-scale LSCs. Their experimental losses in a 1D LSC are almost completely negligible over extremely large waveguide lengths of up to 120 cm. Moreover, these Yb^{3+}:$CsPbCl_3$ NCs display the unusual and

extremely attractive characteristic of quantum cutting, by which PLQYs vastly exceeding 100% have been measured. As demonstrated experimentally in Figures 2-4, however, the PL of these quantum-cutting NCs is absorbed by overtones of high-frequency proton-stretching vibrations present in common LSC polymer matrices.[19-22, 25-30, 35, 36, 38-40, 66, 69, 70, 72] This works shows that to succeed, an LSC based on Yb^{3+}-doped NCs must use a waveguide matrix that contains very few protons in the form of C-H, O-H, or related bonds. Several proven possibilities already exist, although formation of NC LSCs out of such matrices has not yet been demonstrated, and costs may escalate too much for some of these options to be commercially attractive. Nonetheless, it is interesting to note that the amorphous fluorinated polymer Cytop[74] is already used in near-IR fiber optics and has a NIR attenuation coefficient that is close to those used in the glass simulations here. Additionally, organic-dye LSCs have been fabricated with partially fluorinated polymers[78, 79] that show reduced C-H overtone absorption. Some work has been done to incorporate PbSe and InAs NCs into a fluorinated, aromatic copolymer.[80] These results suggest that NC LSCs using fluorinated waveguides are indeed viable and should be developed further. Alternatively, all-inorganic waveguides such as the oxide matrices used for Nd^{3+} LSCs[1, 81] are also attractive; NC LSCs of this type have not yet been demonstrated, but a notable proof-of-concept is found in the examples of colored Schott glasses, which are composed of chalcogenide semiconductor NCs embedded within optical-quality borosilicate glass. High-efficiency Yb^{3+}-doped fiber lasers and amplifiers involving various oxide and fluoride glass compositions with low cavity losses have also been demonstrated.[82, 83]

Conclusion

Through a combination of experimental and computational studies, we have shown that

Yb^{3+}:$CsPb(Cl_{1-x}Br_x)_3$ NCs have high potential to serve as a unique LSC luminophore due to their large effective Stokes shift and extraordinarily high PLQY (approaching 200%), arising from their efficient quantum-cutting PL mechanism. These NCs have the lowest self-absorption of any NCs investigated to date, comparable to Mn^{2+}-doped II-VI NCs, but with overall LSC performance exceeding that of the Mn^{2+}-doped NCs because of their very high PLQYs. The experimental measurements presented here highlight the need for proton-free waveguide matrices in LSCs involving these luminophores, which motivates development of NC LSCs with waveguides based on inorganic glasses or fluorinated polymers. Finally, we propose and model a new monolithic bilayer LSC device architecture containing quantum-cutting Yb^{3+}:$CsPb(Cl_{1-x}Br_x)_3$ NCs in its top layer and, *e.g.*, $CuInS_2$/ZnS NCs in its bottom layer. This bilayer design is reminiscent of tandem PVs and LSCs, except that it uses quantum cutting to increase photocurrent rather than using multiple PV energy gaps to increase photovoltage. As such, this bilayer device has the distinct advantage that PL from both the top (blue-absorbing) and bottom (red-absorbing) luminescent layers can be transported through the same waveguide to the same Si PV, obviating the need for multiple PV cells, interlayer wiring, and current matching as found in traditional tandem devices. Such advantages simplify device construction and operation. Modeling suggests that a bilayer LSC using Yb^{3+}:$CsPb(Cl_{0.25}Br_{0.75})_3$ NCs for the top layer could improve upon the performance of an idealized state-of-the-art $CuInS_2$/ZnS NC LSC bottom layer by at least 19%. It is possible that better inorganic or organic luminophores will be identified in the future to serve as partners with Yb^{3+}:$CsPb(Cl_{0.25}Br_{0.75})_3$ NCs in such bilayer configurations. Overall, these results and the new proposed device structure suggest promising avenues for the development of next-generation NC LSCs.

Acknowledgments. This research was supported by the National Science Foundation (NSF) through the UW Molecular Engineering Materials Center, a Materials Research Science and Engineering Center (DMR-1719797, to DRG and CKL), and through DMR-1807394 (to DRG). This work was also supported by the UW Clean Energy Institute and the Washington Research Foundation. Part of this work was conducted at the UW Molecular Analysis Facility, a National Nanotechnology Coordinated Infrastructure site supported in part by the NSF (ECC-1542101), the University of Washington, the Molecular Engineering and Sciences Institute, the Clean Energy Institute, and the National Institutes of Health. The authors gratefully acknowledge Kyle Kluherz for providing TEM images and Liam Bradshaw for providing 1D LSC attenuation data and for helpful discussion. We also acknowledge Prof. Gerd Bacher, Christian Erickson, and Matt Crane for helpful discussions.

† Electronic supplementary information (ESI) available. See DOI:XX

References

1. W. H. Weber and J. Lambe, *Appl. Opt., AO*, 1976, **15**, 2299-2300.
2. A. Goetzberger and W. Greube, *Appl. Phys.*, 1977, **14**, 123-139.
3. M. G. Debije and P. P. C. Verbunt, *Adv Energy Mater*, 2012, **2**, 12-35.
4. F. Meinardi, F. Bruni and S. Brovelli, *Nat Rev Mater*, 2017, **2**, 17072.
5. B. McKenna and R. C. Evans, *Adv. Mater.*, 2017, **29**, 1606491.
6. P. Moraitis, R. E. I. Schropp and W. G. J. H. M. van Sark, *Opt. Mater.*, 2018, **84**, 636-645.
7. Y. Zhou, H. Zhao, D. Ma and F. Rosei, *Chem. Soc. Rev.*, 2018, **47**, 5866-5890.
8. E. Yablonovitch, *J. Opt. Soc. Am., JOSA*, 1980, **70**, 1362-1363.
9. G. Smestad, H. Ries, R. Winston and E. Yablonovitch, *Sol. Energy Mater*, 1990, **21**, 99-111.
10. H.-J. Song, B. G. Jeong, J. Lim, D. C. Lee, W. K. Bae and V. I. Klimov, *Nano Lett.*, 2018, **18**, 395-404.
11. V. I. Klimov, T. A. Baker, J. Lim, K. A. Velizhanin and H. McDaniel, *ACS Photonics*, 2016, **3**, 1138-1148.
12. Y.-B. Cheng, A. Pascoe, F. Huang and Y. Peng, *Nat News*, 2016, **539**, 488.
13. K. A. Mazzio and C. K. Luscombe, *Chem. Soc. Rev.*, 2014, **44**, 78-90.
14. J. Zhang, M. Wang, Y. Zhang, H. He, W. Xie, M. Yang, J. Ding, J. Bao, S. Sun and C. Gao, *Sol. Energy*, 2015, **117**, 260-267.
15. F. M. Vossen, M. P. J. Aarts and M. G. Debije, *Energ. Buildings*, 2016, **113**, 123-132.
16. A. Reinders, M. G. Debije and A. Rosemann, *IEEE J. Photovolt.*, 2017, **7**, 1663-1666.
17. W. v. Sark, P. Moraitis, C. Aalberts, M. Drent, T. Grasso, Y. L'Ortije, M. Visschers, M. Westra, R. Plas and W. Planje, *Sol. RRL*, 2017, **1**, 1600015.
18. K. Barnham, J. L. Marques, J. Hassard and P. O'Brien, *Appl. Phys. Lett.*, 2000, **76**, 1197-1199.

19. G. V. Shcherbatyuk, R. H. Inman, C. Wang, R. Winston and S. Ghosh, *Appl. Phys. Lett.*, 2010, **96**, 191901.
20. S. R. Wilton, M. R. Fetterman, J. J. Low, G. You, Z. Jiang and J. Xu, *Opt. Express, OE*, 2014, **22**, A35-A43.
21. Y. Zhou, D. Benetti, Z. Fan, H. Zhao, D. Ma, A. O. Govorov, A. Vomiero and F. Rosei, *Adv. Energy Mater.*, 2016, **6**, 1501913.
22. D. L. Waldron, A. Preske, J. M. Zawodny, T. D. Krauss and M. C. Gupta, *Nanotechnology*, 2017, **28**, 095205.
23. F. Meinardi, S. Ehrenberg, L. Dhamo, F. Carulli, M. Mauri, F. Bruni, R. Simonutti, U. Kortshagen and S. Brovelli, *Nat Photon*, 2017, **11**, 177–185.
24. Z. Krumer, S. J. Pera, V. R. J.A. Dijk-Moes, Y. Zhao, D. A. F.P. Brouwer, E. Groeneveld, V. W. G.J.H.M. Sark, R. E. I. Schropp and D. C. Mello Donegá, *Sol. Energy Mater Sol. Cells*, 2014, **111**, 57-65.
25. I. Coropceanu and M. G. Bawendi, *Nano Lett.*, 2014, **14**, 4097-4101.
26. F. Meinardi, A. Colombo, K. A. Velizhanin, R. Simonutti, M. Lorenzon, L. Beverina, R. Viswanatha, V. I. Klimov and S. Brovelli, *Nat. Photon.*, 2014, **8**, 392-399.
27. D. R. Needell, O. Ilic, C. R. Bukowsky, Z. Nett, L. Xu, J. He, H. Bauser, B. G. Lee, J. F. Geisz, R. G. Nuzzo, A. P. Alivisatos and H. A. Atwater, *IEEE J. Photovolt.*, 2018, **8**, 1-8.
28. S. Sadeghi, H. Bahmani Jalali, R. Melikov, B. Ganesh Kumar, M. Mohammadi Aria, C. W. Ow-Yang and S. Nizamoglu, *ACS Appl. Mater. Interfaces*, 2018, **10**, 12975-12982.
29. N. D. Bronstein, L. Li, L. Xu, Y. Yao, V. E. Ferry, A. P. Alivisatos and R. G. Nuzzo, *ACS Nano*, 2014, **8**, 44-53.
30. C. S. Erickson, L. R. Bradshaw, S. McDowall, J. D. Gilbertson, D. R. Gamelin and D. L. Patrick, *ACS Nano*, 2014, **8**, 3461-3467.
31. L. R. Bradshaw, K. E. Knowles, S. McDowall and D. R. Gamelin, *Nano Lett.*, 2015, **15**, 1315-1323.
32. K. E. Knowles, T. B. Kilburn, D. G. Alzate, S. McDowall and D. R. Gamelin, *Chem. Commun.*, 2015, **51**, 9129-9132.
33. X. Hu, R. Kang, Y. Zhang, L. Deng, H. Zhong, B. Zou and L.-J. Shi, *Opt. Express*, 2015, **23**, A858-A867.
34. F. Meinardi, H. McDaniel, F. Carulli, A. Colombo, K. A. Velizhanin, N. S. Makarov, R. Simonutti, V. I. Klimov and S. Brovelli, *Nat. Nanotechnol.*, 2015, **10**, 878-885.
35. C. Li, W. Chen, D. Wu, D. Quan, Z. Zhou, J. Hao, J. Qin, Y. Li, Z. He and K. Wang, *Scientific Reports*, 2015, **5**, 17777.
36. F. Meinardi, Q. A. Akkerman, F. Bruni, S. Park, M. Mauri, Z. Dang, L. Manna and S. Brovelli, *ACS Energy Lett.*, 2017, **2**, 2368-2377.
37. M. Sharma, K. Gungor, A. Yeltik, M. Olutas, B. Guzelturk, Y. Kelestemur, T. Erdem, S. Delikanli, J. R. McBride and H. V. Demir, *Adv. Mater.*, 2017, **29**, 1700821.
38. R. Sumner, S. Eiselt, T. B. Kilburn, C. Erickson, B. Carlson, D. R. Gamelin, S. McDowall and D. L. Patrick, *J. Phys. Chem. C*, 2017, **121**, 3252-3260.
39. M. R. Bergren, N. S. Makarov, K. Ramasamy, A. Jackson, R. Guglielmetti and H. McDaniel, *ACS Energy Lett.*, 2018, **3**, 520-525.
40. K. Wu, H. Li and V. I. Klimov, *Nat. Photon.*, 2018, **12**, 105-110.
41. K. E. Knowles, K. H. Hartstein, T. B. Kilburn, A. Marchioro, H. D. Nelson, P. J. Whitham and D. R. Gamelin, *Chem. Rev.*, 2016, **116**, 10820-10851.

42. A. Marchioro, P. J. Whitham, K. E. Knowles, T. B. Kilburn, P. J. Reid and D. R. Gamelin, *J. Phys. Chem. C*, 2016, **120**, 27040-27049.
43. H. D. Nelson, X. Li and D. R. Gamelin, *J. Phys. Chem. C*, 2016, **120**, 5714-5723.
44. K. E. Hughes, K. H. Hartstein and D. R. Gamelin, *ACS Nano*, 2018, **12**, 718-728.
45. H. D. Nelson and D. R. Gamelin, *J. Phys. Chem. C*, 2018, **122**, 18124-18133.
46. C. Parent, C. Lurin, G. Le Flem and P. Hagenmuller, *J. Lumin.*, 1986, **36**, 49-55.
47. A. Sanguineti, A. Monguzzi, G. Vaccaro, F. Meinardi, E. Ronchi, M. Moret, U. Cosentino, G. Moro, R. Simonutti, M. Mauri, R. Tubino and L. Beverina, *Phys. Chem. Chem. Phys.*, 2012, **14**, 6452-6455.
48. T.-C. Liu, G. Zhang, X. Qiao, J. Wang, H. J. Seo, D.-P. Tsai and R.-S. Liu, *Inorg. Chem.*, 2013, **52**, 7352-7357.
49. P. Liu, J. Liu, X. Zheng, H. Luo, X. Li, Z. Yao, X. Yu, X. Shi, B. Hou and Y. Xia, *J. Mater. Chem. C*, 2014, **2**, 5769-5777.
50. A. K. Rufino Souza, A. P. Langaro, J. R. Silva, F. B. Costa, K. Yukimitu, J. C. Silos Moraes, L. Antonio de Oliveira Nunes, L. Humberto da Cunha Andrade and S. M. Lima, *J Alloys Compd.*, 2019, **781**, 1119-1126.
51. R. Martín-Rodríguez, R. Geitenbeek and A. Meijerink, *J. Am. Chem. Soc.*, 2013, **135**, 13668-13671.
52. S. E. Creutz, R. Fainblat, Y. Kim, M. C. De Siena and D. R. Gamelin, *J. Am. Chem. Soc.*, 2017, **139**, 11814-11824.
53. J. K. Swabeck, S. Fischer, N. D. Bronstein and A. P. Alivisatos, *J. Am. Chem. Soc.*, 2018, **140**, 9120-9126.
54. D. Zhou, D. Liu, G. Pan, X. Chen, D. Li, W. Xu, X. Bai and H. Song, *Adv. Mater.*, 2017, **29**, 1704149.
55. T. J. Milstein, D. M. Kroupa and D. R. Gamelin, *Nano Lett.*, 2018, **18**, 3792–3799.
56. D. M. Kroupa, J. Y. D. Roh, T. J. Milstein, S. E. Creutz and D. R. Gamelin, *ACS Energy Lett.*, 2018, **3**, 2390-2395.
57. A. D. Vos, *J. Phys. D: Appl. Phys.*, 1980, **13**, 839.
58. K. A. Bertness, S. R. Kurtz, D. J. Friedman, A. E. Kibbler, C. Kramer and J. M. Olson, *Appl. Phys. Lett.*, 1994, **65**, 989-991.
59. G. E. Eperon, T. Leijtens, K. A. Bush, R. Prasanna, T. Green, J. T.-W. Wang, D. P. McMeekin, G. Volonakis, R. L. Milot, R. May, A. Palmstrom, D. J. Slotcavage, R. A. Belisle, J. B. Patel, E. S. Parrott, R. J. Sutton, W. Ma, F. Moghadam, B. Conings, A. Babayigit, H.-G. Boyen, S. Bent, F. Giustino, L. M. Herz, M. B. Johnston, M. D. McGehee and H. J. Snaith, *Science*, 2016, **354**, 861-865.
60. K. A. Bush, A. F. Palmstrom, Z. J. Yu, M. Boccard, R. Cheacharoen, J. P. Mailoa, D. P. McMeekin, R. L. Z. Hoye, C. D. Bailie, T. Leijtens, I. M. Peters, M. C. Minichetti, N. Rolston, R. Prasanna, S. Sofia, D. Harwood, W. Ma, F. Moghadam, H. J. Snaith, T. Buonassisi, Z. C. Holman, S. F. Bent and M. D. McGehee, *Nat Energy*, 2017, **2**, 17009.
61. S. Essig, C. Allebé, T. Remo, J. F. Geisz, M. A. Steiner, K. Horowitz, L. Barraud, J. S. Ward, M. Schnabel, A. Descoeudres, D. L. Young, M. Woodhouse, M. Despeisse, C. Ballif and A. Tamboli, *Nat Energy*, 2017, **2**, 17144.
62. A. A. Earp, G. B. Smith, J. Franklin and P. Swift, *Sol. Energy Mater Sol. Cells*, 2004, **84**, 411-426.
63. M. J. Currie, J. K. Mapel, T. D. Heidel, S. Goffri and M. A. Baldo, *Science*, 2008, **321**, 226-228.

64. J. C. Goldschmidt, M. Peters, A. Bösch, H. Helmers, F. Dimroth, S. W. Glunz and G. Willeke, *Sol. Energy Mater Sol. Cells*, 2009, **93**, 176-182.
65. US8866001 B1, 2014.
66. H. Zhao, D. Benetti, X. Tong, H. Zhang, Y. Zhou, G. Liu, D. Ma, S. Sun, Z. M. Wang, Y. Wang and F. Rosei, *Nano Energy*, 2018, **50**, 756-765.
67. T. J. Milstein, K. T. Kluherz, D. M. Kroupa, C. S. Erickson, J. J. De Yoreo and D. R. Gamelin, *Nano Lett.*, 2019, **19**, 1931-1937.
68. Reference Air Mass 1.5 Spectra | Grid Modernization | NREL, https://www.nrel.gov/grid/solar-resource/spectra-am1.5.html.
69. H. Zhao, Y. Zhou, D. Benetti, D. Ma and F. Rosei, *Nano Energy*, 2017, **37**, 214-223.
70. J. Shu, X. Zhang, P. Wang, R. Chen, H. Zhang, D. Li, P. Zhang and J. Xu, *Physica B*, 2018, **548**, 53-57.
71. K. Nikolaidou, S. Sarang, C. Hoffman, B. Mendewala, H. Ishihara, J. Q. Lu, B. Ilan, V. Tung and S. Ghosh, *Adv. Opt. Mater.*, 2016, **4**, 2126-2132.
72. X. Luo, T. Ding, X. Liu, Y. Liu and K. Wu, *Nano Lett.*, 2019, **19**, 338-341.
73. W. Groh, *Die Makromol. Chemie*, 1988, **189**, 2861-2874.
74. S. C. J. Lee, DOI: 10.6100/IR656509, Eindhoven University of Technology, 2009.
75. Schott Optical Glass Collection Datasheet, https://www.us.schott.com/advanced_optics.
76. S. E. Creutz, E. N. Crites, M. C. De Siena and D. R. Gamelin, *Chem. Mater.*, 2018, **30**, 4887–4891.
77. Copper Indium DiSulfide/Zinc Sulfide Quantum Dots, https://www.strem.com/ubiqd.
78. G. Griffini, M. Levi and S. Turri, *Sol. Energy Mater Sol. Cells*, 2013, **118**, 36-42.
79. D. Pintossi, S. Turri, G. Griffini, A. Colombo and C. Dragonetti, 2017 IEEE International Conference on Environment and Electrical Engineering and 2017 IEEE Industrial and Commercial Power Systems Europe, 2017.
80. Y. K. Olsson, G. Chen, R. Rapaport, D. T. Fuchs, V. C. Sundar, J. S. Steckel, M. G. Bawendi, A. Aharoni and U. Banin, *Appl. Phys. Lett.*, 2004, **85**, 4469-4471.
81. B. Jeżowska-Trzebiatowska, E. Łukowiak, W. Stręk, A. Buczkowski, S. Patela, J. Radojewski and J. Sarzyński, *Sol. Energy Mater*, 1986, **13**, 267-277.
82. L. Goldberg, J. P. Koplow and D. A. V. Kliner, *Opt. Lett., OL*, 1999, **24**, 673-675.
83. R. Paschotta, J. Nilsson, A. C. Tropper and D. C. Hanna, *IEEE Journal of Quantum Electronics*, 1997, **33**, 1049-1056.

TOC Graphic and Sentence

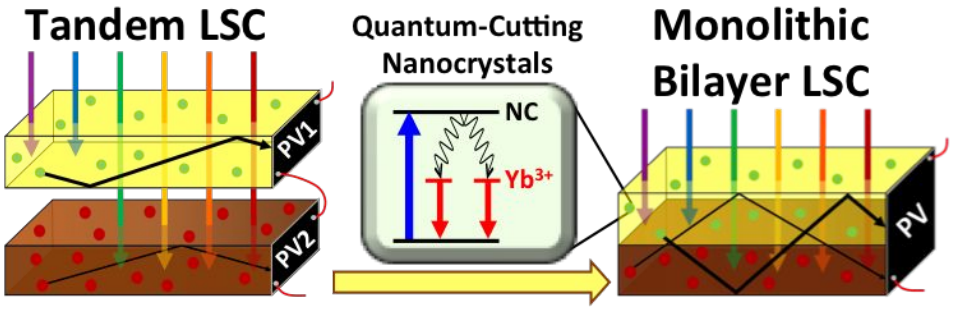

Quantum-cutting Yb^{3+}:$CsPb(Cl_{1-x}Br_x)_3$ nanocrystals mitigate thermalization and reabsorption losses in a new monolithic bilayer luminescent solar concentrator device architecture.